ACS APPLIED MATERIALS & INTERFACES

Research Article

www.acsami.org

PdNi Hollow Nanoparticles for Improved Electrocatalytic Oxygen Reduction in Alkaline Environments

Meng Wang,[†] Weimin Zhang,[‡] Jiazhao Wang,[§] David Wexler,[∥] Simon D. Poynton,[⊥] Robert C.T. Slade,[⊥] Huakun Liu,[‡] Bjorn Winther-Jensen,[#] Robert Kerr,[#] Dongqi Shi,[§] and Jun Chen*[,†]

[†]ARC Centre of Excellence for Electromaterials Science, Intelligent Polymer Research Institute, Australian Institute of Innovative Materials, University of Wollongong, Wollongong, NSW 2500, Australia

[‡]Shanghai Sinopoly Batteries Research Institute, Shanghai 200241, China

[§]Institute for Superconducting and Electronic Materials, University of Wollongong, Wollongong, NSW 2500, Australia

[∥]School of Mechanical, Materials and Mechatronic Engineering, University of Wollongong, Wollongong, NSW 2500, Australia

[⊥]Department of Chemistry, University of Surrey, Guildford, Surrey GU2 7XH, United Kingdom

[#]Department of Materials Engineering, Monash University, Clayton, VIC 3800, Australia

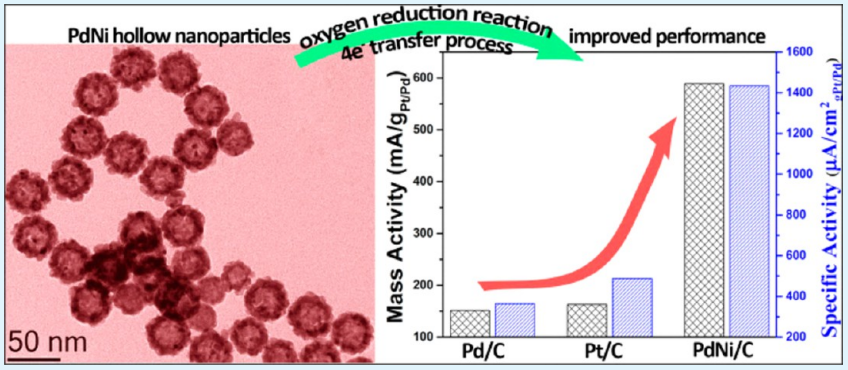

ABSTRACT: Palladium-nickel (PdNi) hollow nanoparticles were synthesized via a modified galvanic replacement method using Ni nanoparticles as sacrificial templates in an aqueous medium. X-ray diffraction and transmission electron microscopy show that the as-synthesized nanoparticles are alloyed nanostructures and have hollow interiors with an average particle size of 30 nm and shell thickness of 5 nm. Compared with the commercially available Pt/C or Pd/C catalysts, the synthesized PdNi/C has superior electrocatalytic performance towards the oxygen reduction reaction, which makes it a promising electrocatalyst for alkaline anion exchange membrane fuel cells and alkali-based air-batteries. The electrocatalyst is finally examined in a H_2/O_2 alkaline anion exchange membrane fuel cell; the results show that such electrocatalysts could work in a real fuel cell application as a more efficient catalyst than state-of-the-art commercially available Pt/C.

KEYWORDS: *palladium nickel, hollow, bimetallic, oxygen reduction reaction, alkaline membrane fuel cell*

1. INTRODUCTION

The oxygen reduction reaction (ORR) has been recognized as the kinetically limiting step in fuel cells and metal-air batteries due to sluggish reaction kinetics.[1,2] Platinum (Pt), the most efficient electrocatalyst for the ORR, is inhibited from large-scale commercialization due to high cost, poor stability, and poor poison resistance.[3−5] It has been well documented that the overpotential for the ORR will be significantly reduced in a high pH (alkaline) environment, thus offering the possibilities of lower usage and wider selection of electrocatalysts other than platinum to be available for this catalytic reaction,[6,7] while recent advances in the development of alkaline anion exchange membranes (AAEMs) have also seen the performance of the anion exchange membrane fuel cell (AEMFC) approach that of the analogous, conventional acidic Nafion proton exchange membrane fuel cell (PEMFC).[8−10] This adds further incentive to the need to develop novel nanostructured electrocatalysts for the ORR in the alkaline medium.

Palladium (Pd), with competitive intrinsic electrocatalytic performance towards the ORR compared to Pt, is less expensive and more abundant and has received considerable attention recently.[7,11−14] Pd alloyed with transition metals (Pd−TMs), such as Pd−Ni,[15,16] Pd−Cu,[17−20] Pd−Fe,[7,21,22] and Pd−Co,[23] has proven to be an effective way to reduce cost and simultaneously to enhance catalytic performance.[7,24] Compared with alloying with noble metals such as Pd−Au[11,25,26] or Pd−Ag,[6,24,27] Pd alloyed with TMs provides a

Received: September 20, 2013
Accepted: November 7, 2013
Published: November 7, 2013

more practical and economical way to produce Pd-based bimetallic electrocatalysts for the ORR in alkaline media.

Among these bimetallic electrocatalysts, hollow structures are proving to be economically viable, while they are also more efficient catalysts due to their higher surface area and catalyst utilization efficiency compared with their filled solid counterparts.[28] The so-called sacrificial template protocol (galvanic replacement), which was first well demonstrated by Xia's group,[29] has been modified and widely applied to synthesize nanocrystals with hollow features.[30] Pt-based bimetallic hollow nanostructures such as Pt−Pd,[5,31] Pt−Ag,[32] and Pt−TMs (Pt−Co,[33,34] Cu,[28] and Ni[35]) with enhanced electrocatalytic performance have been reported. In comparison with the development of Pt-bimetallic hollow nanostructures, reports on synthesizing Pd-based bimetallic hollow nanostructures have been rare, mainly because the activity and the durability of Pd in the ORR are poor in acidic media.[7] For example, Pd−Ag hollow nanorings were synthesized with good methanol tolerance,[27] while the ORR performance was not improved, mainly because the larger lattice constant of silver would subject the Pd to a tensile strain effect, decreasing the electroactivity of Pd towards the ORR.[36] Pd−Co[37] and Pd−Cu[38] hollow nanostructures were also reported with large particle size (>50 nm), but their ORR properties were not extensively studied due to the large particle size, which may decrease the active surface area. Thus, there is still an urgent need to develop Pd−TM bimetallic hollow nanostructures with catalytic oxygen reduction abilities in alkaline media.

In this report, we present novel hollow PdNi nanostructures synthesized via a modified galvanic process using Ni nanoparticles as sacrificial templates in aqueous solution. Electrochemical testing to investigate the ORR effects showed that the as-synthesized PdNi had an outstandingly high mass activity of 588.97 mA g^{-1}_{Pd}, which is 3.9 times higher than that of Pt/C, when the precursor ratio of Pd:Ni was 1:1 (denoted as Pd_1Ni_1 in this report) at −0.114 V (vs Ag/AgCl). Together with single H_2/O_2 fuel cell testing, it is evidenced that Pd_1Ni_1/C could serve as an efficient and durable AEMFC electrocatalyst in a practical working device.

2. EXPERIMENTAL SECTION

Chemicals. Nickel(II) chloride hexahydrate ($NiCl_2·6H_2O$), palladium(II) chloride ($PdCl_2$), sodium citrate (99%), and sodium borohydride ($NaBH_4$, 99.99%) were purchased from Sigma-Aldrich. Carbon black (CB, Vulcan XC-72 R) was provided by the Cabot Corporation. All glassware and PTFE-coated magnetic stir bars were cleaned with aqua regia, followed by copious rinsing with distilled water before drying in an oven.

Synthesis. Ni nanoparticles were synthesized using the borohydride reduction method. Briefly, 0.02 mmol of $NiCl_2·6H_2O$ and 29.4 mg of sodium citrate were added to 40 mL of distilled water. After deoxygenating with nitrogen for 15 min, 2 mL of freshly prepared $NaBH_4$ (7.5 mg) was injected into the solution by syringe. The color of the solution immediately turned dark yellow after the addition of $NaBH_4$, indicating the formation of Ni nanoparticles. After a few minutes, 0.02 mmol of H_2PdCl_4 in 40 mL of deoxygenated water was added dropwise into the Ni particle/colloid at a rate of 1 mL min^{-1} and allowed to react for another 2 h. The synthesized PdNi nanoparticles were supported on carbon black (CB, Vulcan XC-72 R, Cabot Corp.) with a loading of 20 mass %, achieved by mixing the above colloids with acid-treated CB. A solid sample was obtained by filtration. Before filtration, an aliquot of sodium hydroxide was added with stirring for another 2 h, and then the products were filtered and rinsed with water several times to remove the residual impurities in the catalysts and then dried at 80 °C overnight. This sample was denoted as Pd_1Ni_1/C. To determine the optimized molar ratio of Pd:Ni, PdNi/C catalysts with various precursor mole ratios of Pd to Ni, 3:1, 2:1, 1:1, and 0.5:1, were synthesized. The corresponding samples were denoted as Pd_3Ni_1/C, Pd_2Ni_1/C, Pd_1Ni_1/C, and $Pd_{0.5}Ni_1/C$, respectively.

Physical Characterization. Low-magnification TEM images were collected with a JEOL JEM-2100F transmission electron microscope (TEM). High-resolution (HR)-TEM images, scanning transmission electron microscope (STEM) images, and probe-corrected energy dispersive spectroscopy (EDS) line scans were collected in high-angle annular dark-field imaging (HAADF)-STEM mode, using a JEOL-JEM 2200FS TEM operated at 200 kV. Samples for TEM were prepared by dropping one drop of the cleaned nanoparticles in ethanol dispersion on a copper grid (200 mesh). The powder X-ray diffraction (XRD) patterns were collected using a Bruker D8-Advance X-ray powder diffractometer with Cu Kα radiation (λ = 1.5406 Å). X-ray photoelectron spectroscopy (XPS) spectra were collected using a Thermo Scientific K-Alpha instrument. Metal contents of the products were determined using inductively coupled plasma−mass spectrometry (ICP−MS 7500CS, Agilent Technologies).

Electrochemical Measurements. Electrochemical measurements were performed using the thin-film rotating-disk electrode (TF-RDE) technique, as reported elsewhere.[39] The thin-film electrode was prepared through placing 10 μL of the catalyst ink on a glassy carbon rotating disk electrode (RDE, 0.1925 cm^2, Pine Research Instrumentation). The electrocatalyst ink was prepared by dispersing the electrocatalyst in Nafion/H_2O/isopropanol (m/m/m = 0.05/10/50) to obtain a 2 mg mL^{-1} dispersion via a sonicator (Brandson). The electrode was then connected to a CHI 720c bipotentiostat (CH Instruments) in a standard three-electrode cell with a Pt-mesh counter electrode and a KCl(aq) saturated (3 mol L^{-1}) Ag/AgCl reference. Unless otherwise specified, all the potentials are against Ag/AgCl as reference potential.

The cyclic voltammetry (CV) traces were recorded in N_2-saturated KOH(aq) (0.1 mol L^{-1}) solution with a sweep rate of 50 mV s^{-1}. The ORR polarization curves were recorded using a linear sweep voltammetry (LSV) technique in oxygen-saturated electrolyte with a sweep rate of 10 mV s^{-1} at various rotation speeds of 100, 400, 900, and 1600 rpm from 0.1 to −0.8 V. Stability tests were carried out by the chronoamperometry technique at the potential of −0.2 V and with rotation at 1600 rpm in oxygen-saturated electrolyte for 8000 s.

Single Fuel Cell Test. The anion-exchange membranes used were electron-beam-grafted EFTE membranes (graft copolymerized) using vinylbenzyl chloride and functionalized using trimethylamine (University of Surrey);[10] the membrane used was of type S80, with membrane thickness ≈80 μm (thickness depends on hydration level) and ion exchange capacity IEC ≈ 1.3 meq g^{-1}. The anodes and cathodes were prepared as described previously.[10] In brief, the electrocatalyst ink with ca. 10 mass % PTFE as binder was firstly sprayed on the gas diffusion layers (GDLs, 5 cm^2) to a loading of 0.4 mg cm^{-2} and was then spray-treated with poly(vinybenzyl chloride) dissolved in ethyl acetate. The prepared GDLs were subsequently immersed in undiluted *N*,*N*,*N*′,*N*′-tetramethylhexane-1,6-diamine (TMEDA) for 24 h and then washed thoroughly with water. The Pt/C was used as the electrocatalysts for anodes. For comparison purposes, the commercial E-Tek Pt/C and the Pd_1Ni_1/C were chosen and used as catalysts for cathodes. Before single fuel cell testing, the AAEMs and GDL electrodes were immersed in KOH(aq) (1 mol L^{-1}) solution for 1 h to give alkaline anion-exchange materials (OH^- conducting polymer electrolyte and cross-linked ionomer). The membrane electrode assemblies (MEAs) were prepared by sandwiching the anode GDLs and the AAEMs and tested using an 850e fuel cell test system (Fuel Cell Technologies, Inc., USA) fed with humidified hydrogen and oxygen. The gas flow was controlled at 0.08 mL min^{-1}. The fuel cell measurements were carried out at 60 °C under 15 psi (103 kPa) back pressure. The polarization curves were recorded using a potential scan method by holding the cell at each potential for 30 s to obtain the steady-state current value with a scan rate of 25 mV s^{-1} from 0.90 to 0.25 V.

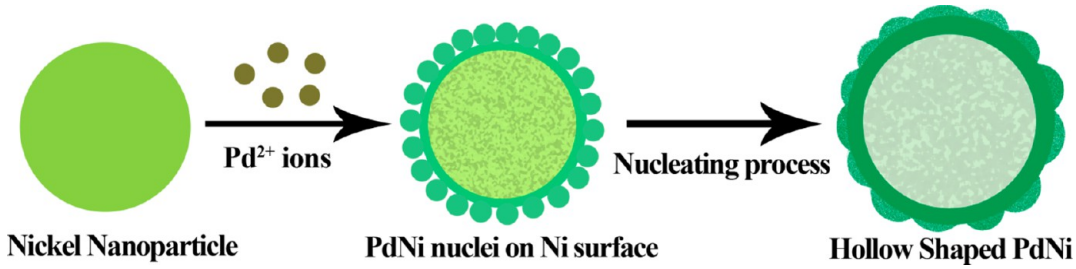

Figure 1. Schematic illustration of the formation of hollow PdNi nanoparticles.

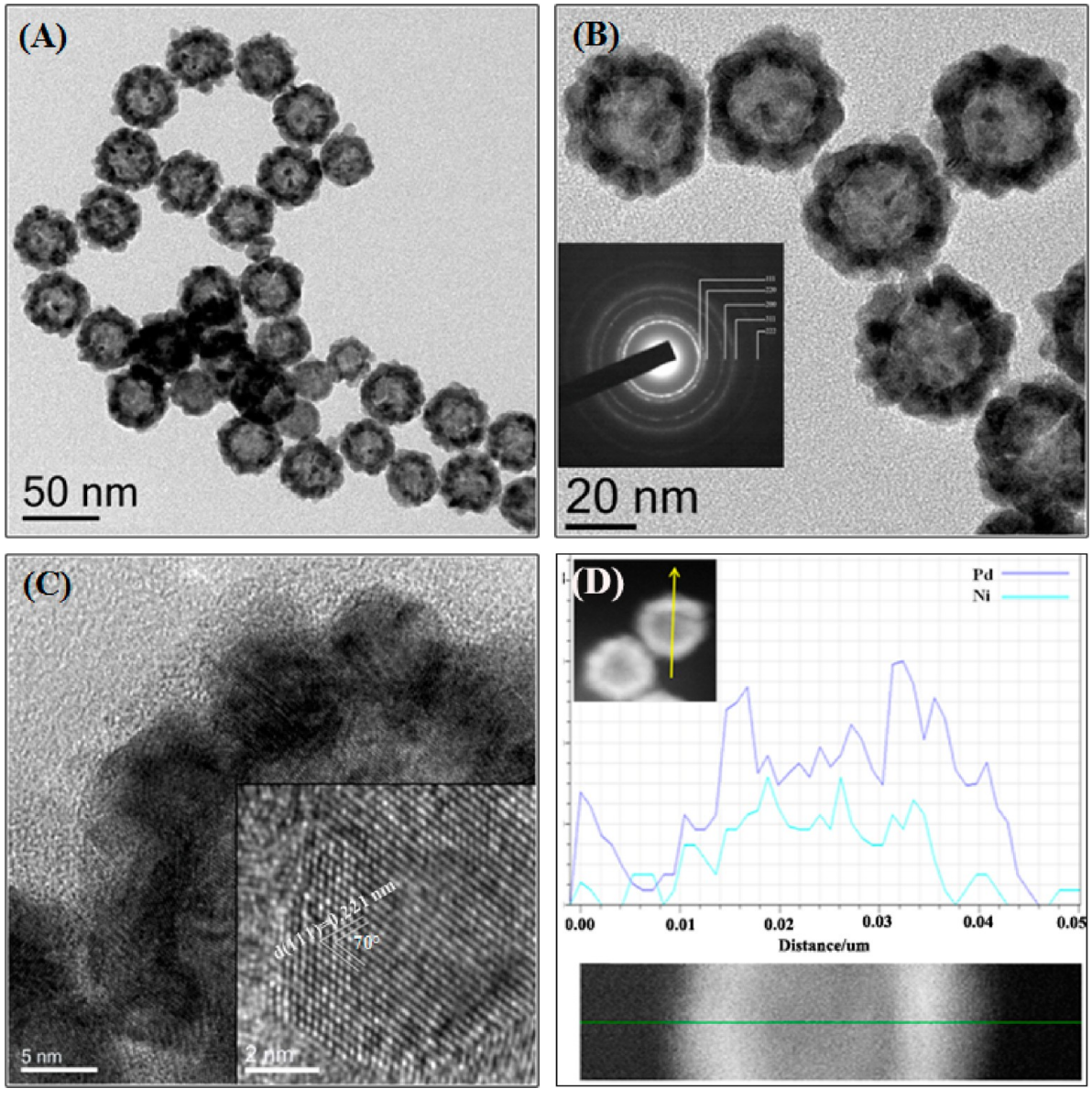

Figure 2. (A) Low-magnification TEM image and (B) high-magnification TEM image of the Pd_1Ni_1 hollow nanoparticles (inset: corresponding SAED pattern); (C) representative high-resolution (HR) TEM image of the hollow PdNi nanoparticles, with the inset showing higher resolution with lattice spacing; and (D) line-scanning profile across a Pd_1Ni_1 hollow nanoparticle (insets: HAADF-STEM images of the scanned nanoparticle).

3. RESULTS AND DISCUSSION

A schematic illustration of the synthesis of PdNi hollow nanoparticles is presented in Figure 1, which is quite similar to the mechanism proposed in our previous work.[40] As the standard reduction potential of Ni(II)/Ni (−0.257 V vs standard hydrogen electrode (SHE)) is lower than that of the $PdCl_4^{2-}$/Pd couple (0.59 V vs SHE), once dihydrogen tetrachloropalladate(II) solution is added the galvanic replacement will occur immediately ($2Ni + PdCl_4^{2-} \rightarrow 2Ni^2 + Pd + 4Cl^-$). In this process, Ni nanoparticles serve as the template and are gradually consumed by Pd salts, thereby forming hollow cores. The Pd(II) ions will be co-reduced with a certain

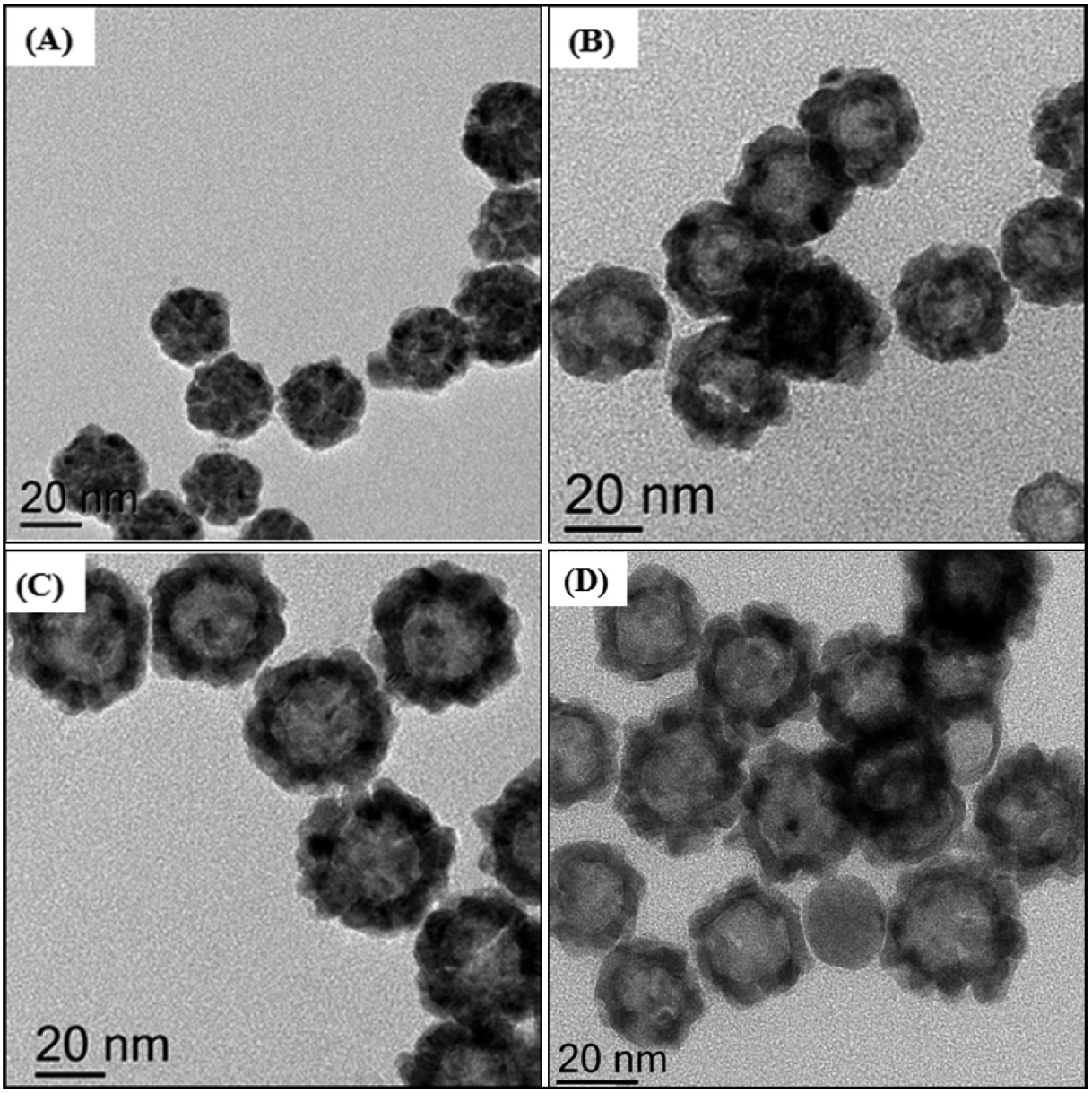

Figure 3. Typical TEM images of PdNi hollow nanoparticles with different Pd/Ni precursor ratios; the molar ratios of Pd/Ni are (A) 3:1, (B) 2:1, (C) 1:1, and (D) 0.5:1.

amount of Ni(II) (leached away during the previous process) and be deposited on the surface of the Ni nanoparticles and form PdNi alloy shells.

Morphologies of the nanoparticles thus produced were examined by TEM (Figure 2(A) and (B)). It is clear that the nanoparticles are mostly well dispersed, with the shell color much darker than the inside core, suggesting hollow-featured nanostructures. The average diameter of the hollow spheres is ca. 30 nm, and the shell thickness is 5−7 nm. Another feature of the hollow nanoparticles is that their shells are constructed from numerous discontinuous grains (crystalline alloy particles) (Figure 1(C)) with an average size of 3−5 nm, which indicates that the shells are incomplete and porous. This mechanism could be explained by the faster reaction kinetics of Pd/Ni, as proposed in our previous report.[40] The selected area electron diffraction (SAED) pattern (inset, Figure 2(B)) indicates that the nanoparticles are polycrystalline nanocrystals with a face-centred-cubic (fcc) structure. The *d*-spacing of lattice fringes determined from the HR-TEM images (Figure 2(C) inset) is 0.221 nm, corresponding to the (111) planes of the PdNi alloy nanostructure. Probe-corrected HAADF-STEM EDS line scan analysis (Figure 2(D)) was further used to determine the elemental distribution within the nanoparticles. As is shown, Pd and Ni are both distributed through the particles, with more Pd aggregated on the shell. In addition, more of the elements were detected on the shell than in the core, reflecting the formation of a hollow shape.

Impacts of the precursors' molar ratio on the morphology of the nanoparticles were carefully examined, as shown in Figure 3. When the precursor ratio Pd/Ni is ≥3, the hollow feature can barely be observed due to the relatively thick shells of the nanoparticles (>10 nm, Figure 3(A)). The shell thickness decreases, and the particle size slightly increases, with reduction of the Pd proportion. As a consequence, well-defined hollow shapes gradually appear. When the ratio of Pd/Ni is 0.5 in the precursor, some smaller nanoparticles with sizes of about 15

nm are also produced (Figure 3(D)), which may be because the Pd ions were insufficient to consume all the Ni nanoparticles to form hollow shapes in the solution, causing the thus-produced nanoparticles to be partially solid. This was evidenced by the single Ni peak on the XRD patterns (Figure 4(A)). The shell porosity was also changed when the ratio in the precursors was varied; with less Pd, the shell tended to be more porous.

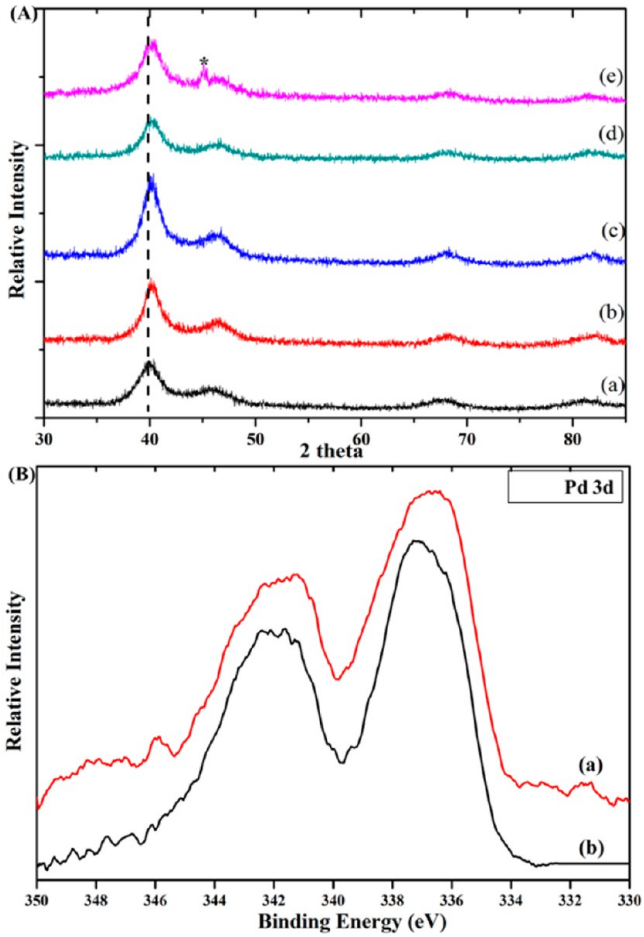

Figure 4. (A) XRD patterns of the synthesized nanoparticles: (a) "homemade" Pd/C, (b–e) PdNi hollow nanoparticles with various Pd/Ni ratios: (b) to (e) Pd_3Ni_1/C, Pd_2Ni_1/C, Pd_1Ni_1/C and $Pd_{0.5}Ni_1/C$; (B) XPS spectra of Pd 3d in (a) Pd_1Ni_1/C and (b) "homemade" Pd/C.

XRD was employed to analyze the crystal structures of the hollow PdNi particles, as shown in Figure 4(A). The diffraction peaks indicated that the structure could be indexed using a face-centred-cubic (fcc) lattice, with (111), (200), (220), and (311) crystal planes forming the facets. In comparison to the pure Pd/C (JCPDS 89-4897), the four characteristic peaks of PdNi/C are noticeably shifted toward higher diffraction angles, suggesting the formation of Pd/Ni alloyed nanostructures. Moreover, a single pure Pd peak was not detected, indicating that all the Pd is in the alloyed state.

Products with various mole ratios were also examined by XRD. The positions of the four characteristic peaks of the PdNi alloyed nanostructures (40.7°, 47.3°, 69.3°, and 82.8° (2θ)) are almost unchanged, regardless of variation in the Pd precursor concentration, revealing that the fractions of Ni atoms alloyed with Pd atoms were the same (~22%, Table 1). A single Ni peak (marked with the star symbol) which could be assigned to the (111) planes of the face-centered-cubic (fcc) nickel (JCPDS No. 04-0850) is detected when the precursor ratio of Pd to Ni is decreased to 0.5:1, revealing that some Ni still remains unconsumed in the final products.

Table 1. Summary of Metal Contents Derived from ICP–MS and XRD

precursors	derived from ICP–MS	derived from XRD[a]		
	Pd/Ni mole ratio	lattice constant (Å)	Pd mole fraction	Pd/Ni mole ratio
3	3.44	3.812	78.92	3.74
2	3.32	3.802	76.22	3.20
1	3.06	3.798	75.13	3.04
0.5	0.53	3.795	74.32	2.89

[a]The lattice parameters were the average lattice spacings calculated from the three major reflections ((111), (200), and (220)) of the alloyed nanoparticles; the Pd molar fractions were obtained assuming Vegard's law.

X-ray photoelectron spectroscopy (XPS) was employed to investigate the electronic environment of Pd in the hollow Pd_1Ni_1 nanoparticles (Figure 4(B)). The two peaks around the binding energies of 341 and 336.5 eV are assigned to the Pd $3d_{3/2}$ (high-energy band) and $3d_{5/2}$ (low-energy band) and reveal that Pd is metallic Pd(0) in the alloyed nanostructures.[41] When compared to data for pure Pd/C, the binding energy is lowered by ca. 0.8 eV, clearly showing the changes in the electronic structure of Pd, possibly due to the charge transfer between Ni and Pd in the alloyed shell.[16]

To determine the metal composition of the hollow nanoparticles, ICP–MS tests were conducted. Table 1 summarizes the metal compositions of the hollow nanoparticles derived from ICP–MS and XRD. The final Pd/Ni ratios in the products are mostly around 3.0–3.7:1, decreasing as the molar ratio of Pd to Ni decreases in the precursor. When the Pd/Ni precursor ratio was 0.5:1, the results derived from XRD show that the Pd/Ni molar ratio is 2.89 in the alloyed PdNi nanoparticles, excluding the presence of Ni nanocrystals. When considering the existence of unconsumed Ni, the ICP–MS shows a more accurate ratio of Pd:Ni, which is about 0.53.

CV traces were obtained and used for a preliminary study of the electrochemical properties of the synthesized Pd_1Ni_1/C, Pd/C, and E-Tek Pt/C (Figure 5(A)). The CVs are consistent with typical characterized CV regimes of Pd or Pt: typical hydrogen underpotential adsorption/desorption peaks in the potential range of −0.9 to −0.6 V; a double-layer capacitance region from −0.6 to −0.4 V; and metal oxidation/reduction peaks in the range between −0.3 and 0.1 V. The electrochemical surface active area (ECSA) was calculated based on the charge transfer in the metal reduction region at around −0.25 (vs Ag/AgCl), subtracting the double-layer correction and assuming 0.405 mC cm^{-2} for the reduction of a monolayer of PdO on the catalyst surface and 0.210 mC cm^{-2} for the reduction of a monolayer of PtO.[7] The ECSAs are 48.1 and 44.5 $m^2\ g^{-1}_{Pd}$ for Pd_1Ni_1/C and Pd/C and 59.7 $m^2\ g^{-1}_{Pt}$ for Pt/C. Although the particle size of Pd_1Ni_1/C is much larger than that for Pd/C, it still shows a slightly higher ECSA than that of the Pd/C, mainly because of its hollow and porous characteristics.

The thin-film rotating-disk electrode (TF-RDE) technique was used to study the ORR activities and kinetics at the

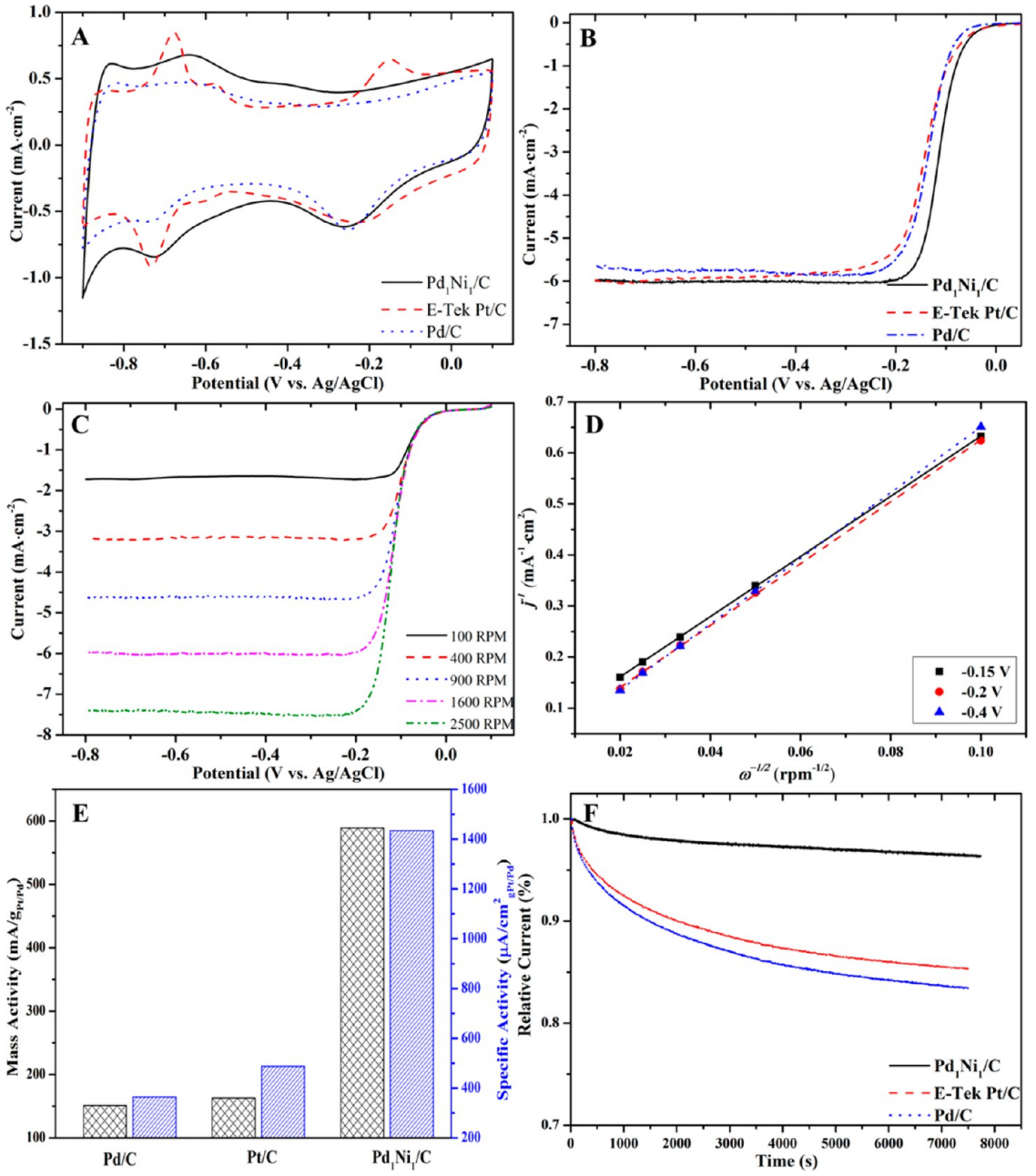

Figure 5. (A) CV traces and (B) ORR polarization curves of the Pd_1Ni_1/C, home-made Pd/C, and commercial E-Tek Pt/C. (C) ORR polarization curves of the Pd_1Ni_1/C at various rotation rates. (D) K–L plots derived from the ORR curves of the Pd_1Ni_1/C at different potentials. (E) Mass activities and specific activities of the Pd1Ni1/C, Pd/C, and E-Tek Pt/C at −0.1 and −0.2 V. (F) Chronoamperometric responses of the electrocatalysts at −0.2 V with rotation rate of 1600 rpm. ORR curves and chronoamperometric responses were measured in O_2-saturated KOH(aq) (0.1 mol L^{-1}) solution with a scan rate of 10 mV s^{-1}.

Pd_1Ni_1/C, Pd/C, and commercial Pt/C electrodes. Figure 5(B) shows the ORR polarization curves of these catalysts obtained at a rotation speed of 1600 rpm. All the polarization curves display a well-defined diffusion-limiting current region from −0.8 to −0.2 V and a mixed kinetic-diffusion control region from 0.05 to −0.2 V. The half-wave potential of the Pd_1Ni_1/C for the ORR is −0.114 V (RSD = 1%), which is slightly higher than that of Pt/C (−0.117 V, RSD = 1%) and much more positive than that of Pd/C (−0.135 V, RSD = 1%), indicating the hollow-shaped Pd_1Ni_1 nanoparticles feature a significant enhancement in the electrocatalytic ORR in an alkaline medium compared with Pd/C or commercial Pt/C.

To obtain the kinetics of the ORR, ORR polarization curves were collected at various rotation speeds (Figure 5(C)), and the corresponding Koutecky–Levich (K–L) plots (Figure 5(D)) were drafted from the ORR polarization curves at different potentials. The number of electrons involved per O_2 molecule reduction can be determined using the Koutecky–Levich (K–L) equation

$$j = 1/j_k + 1/B\omega^{0.5}$$

$$[B = 0.2nF(D_{O2})^{2/3}(v)^{-1/6}C_{O2}]$$

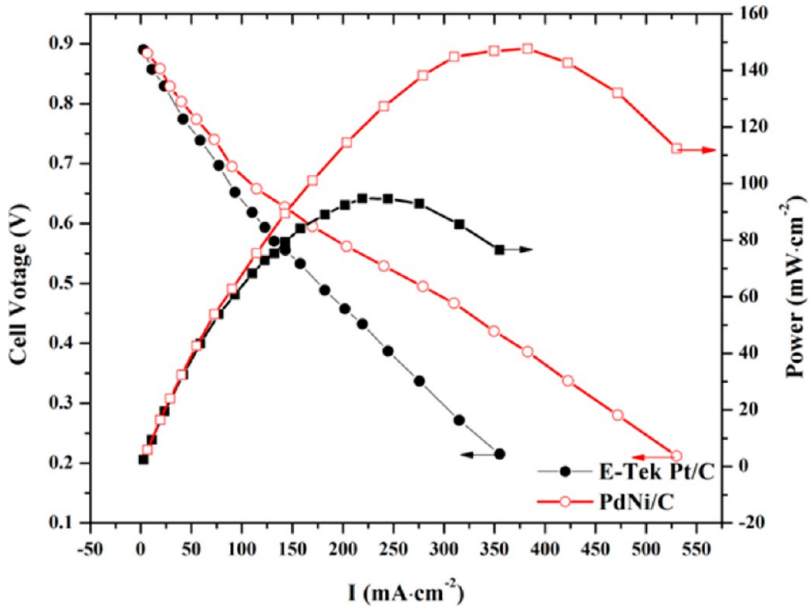

Figure 6. AEMFC polarization curves (round symbols) and power density curves (square symbols) of a single cell test using E-Tek Pt/C (filled symbols) and PdNi/C (hollow symbols) as cathode catalysts with a loading amount of 0.4 mg cm^{-2}. Operating conditions: cell temperature 60 °C, humidifier temperatures 60° C for both H_2 and O_2, flow rate 0.08 L min^{-1}, and back pressure 15 psi for both H_2 and O_2.

where j_k is the kinetic current; ω is the electrode rotation rate; n is the transferred electron number; F is the Faraday constant (F = 96485 C mol^{-1}); D_{O2} is the diffusion coefficient of O_2 = 1.9 × 10^{-5} cm^2 s^{-1}; υ is the kinetic viscosity (0.01 cm^2 s^{-1}); and C_{O2} is the bulk concentration of O_2 (1.2 × 10^{-6} mol cm^{-3}). The constant 0.2 is adopted when the rotation speed is expressed in rpm. The transferred electron number was calculated to be 4.20−4.40 at around −0.15 to −0.4 V, revealing that the ORR from 0.15 to −0.4 V is dominated by a four-electron (4e) pathway and that O_2 is reduced to OH^- during the reaction.

To study the electroactivities of the PdNi/C, Pd/C, and Pt/C in detail, the kinetic current has been calculated from the ORR polarization curves by considering the mass-transport correction using the Levich−Koutecky equation ($1/i_k + 1/i_d$, where i_k is the kinetic current and i_d is the diffusion-limited current), which is normalized against and then normalized to the mass and specific area of Pd or Pt to compare the mass activities and specific area activities of the catalysts. The mass activity and the specific area activity of the Pd_1Ni_1/C is 588.97 mA g^{-1}_{Pd} and 1434 μA cm^{-2}, which is 3.89 and 3.92 times higher than those of Pt/C or Pd/C, respectively, indicating the significant improvement of ORR catalytic activity for the hollow Pd_1Ni_1. The ORR activities of the other products were also examined. The mass activities were 304.85, 272.43, and 184.41 mA g^{-1}_{Pd}, and the specific area activities were 721.6, 849.1, and 1097 μA cm^{-2} for $Pd_{0.5}Ni_1$/C, Pd_2Ni_1/C, and Pd_3Ni_1/C, respectively, at −0.114 V (vs Ag/AgCl). Comparing with Pt/C (151.3 mA g^{-1}_{Pt}) or Pd/C (162.96 mA g^{-1}_{Pd}), we infer that the enhanced ORR activity of the PdNi/C can be ascribed to the unique hollow alloyed structures with porous shells of nanoparticles. Moreover, the changes in the surface electronic features through the introduction of a second metal to Pd would also contribute to the increased activity.[7] As suggested in the XRD patterns (Figure 4(A)), the alloyed PdNi nanoparticles with a slightly smaller lattice parameter will cause the compressed surface strain effect on the Pd skin (suggested in Figure 4(B)) which is beneficial for the oxygen reduction reaction.[7,42]

A chronoamperometric study was conducted to determine the durability of the catalyst for the ORR (Figure 5(F)). During the long (∼8000 s) ORR test at −0.2 V, a 5% current loss for the hollow-shaped Pd_1Ni_1/C was observed. In contrast, for Pd/C or commercial Pt/C, the current losses under identical conditions are more than 10%. These results clearly indicate the hollow PdNi/C is much more stable than the commercial Pt/C or Pd/C in terms of the catalytic activities of oxygen.

The TF-RDE technique is useful for identifying candidate materials, but tests operated under conditions that are much closer to fuel cell operating conditions are necessary to demonstrate the practical performances of the electrocatalysts. Anion exchange membrane fuel cell tests as described previously[10] were carried out to evaluate the performance of the catalysts in a practical environment. Figure 6 shows the polarization curves and power density curves of AEMFC tests with commercial E-Tek Pt/C and Pd_1Ni_1/C cathode catalysts, respectively. The peak power density obtained with the commercial E-Tek Pt/C electrocatalysts is 90 mW cm^{-2} at the loading of 0.4 mg cm^{-2}, which is compatible to the previous results.[10] Under the same testing conditions, the hollow Pd_1Ni_1/C electrode exhibits much higher power density and current density than those with Pt/C. The peak power density of the hollow Pd_1Ni_1/C electrode obtained at 0.4 V is 150 mW cm^{-2}, which is more than 1.7 times higher than that with the commercial Pt/C (90 mW/cm^2). In addition, at 0.4 V the current density of the hollow Pd_1Ni_1/C is 375 mA cm^{-2}, which is 1.5 times larger than that of the Pt/C at the same voltage (current then 240 mA cm^{-2}). These results, which are consistent with the RDE results (Figure 5), provide clear evidence to suggest that the Pd_1Ni_1/C electrocatalysts have the potential to perform as more promising and efficient electrocatalysts in alkaline membrane fuel cells (a working, real environment) when compared with state-of-the-art commercial Pt/C electrocatalysts.

4. CONCLUSION

We have described a modified galvanic replacement method to synthesize hollow PdNi nanoparticles with superior ORR electrocatalytic performance in an alkaline environment. XRD, TEM, and HR-TEM images show that the synthesized hollow nanoparticles are alloyed nanostructures with an average size of 30 nm and a shell thickness of 5 nm. Electrochemical tests have revealed that the PdNi hollow nanoparticles are superior ORR catalysts when compared to commercial Pt/C or Pd/C. The improved performance is assigned to the unique hollow porous structure and changes in the electronic structures when a second metal (Ni) is introduced in addition to the Pd. Moreover, practical fuel cell tests have revealed that PdNi catalysts, with much lower cost, could work as more efficient catalysts than commercial Pt/C under real operating conditions. This method could be used to synthesize other Pd-based hollow nanostructured electrocatalysts with low cost and high catalytic performance for future AEMFCs.

AUTHOR INFORMATION

Corresponding Author

*E-mail: junc@uow.edu.au.

Notes

The authors declare no competing financial interest.

ACKNOWLEDGMENTS

The authors acknowledge the continuous financial support by Australian Research Council Centre of Excellence for Electromaterials Science (ACES) and ARC DP110103909, the Australian National Fabrication Facility (ANFF) for provision of services and equipment access, and the use of facilities within the UOW Electron Microscopy Centre. Work on energy materials and functional devices at the University of Surrey is funded by the UK's Engineering and Physical Sciences Research Council (EPSRC).

REFERENCES

(1) Wu, G.; MacK, N. H.; Gao, W.; Ma, S.; Zhong, R.; Han, J.; Baldwin, J. K.; Zelenay, P. *ACS Nano* **2012**, *6*, 9764−9776.
(2) Debe, M. K. *Nature* **2012**, *486*, 43−51.
(3) Lim, B.; Jiang, M.; Camargo, P. H. C.; Cho, E. C.; Tao, J.; Lu, X.; Zhu, Y.; Xia, Y. *Science* **2009**, *324*, 1302−1305.
(4) Wang, S.; Iyyamperumal, E.; Roy, A.; Xue, Y.; Yu, D.; Dai, L. *Angew. Chem., Int. Ed.* **2011**, *50*, 11756−11760.
(5) Hong, J. W.; Kang, S. W.; Choi, B. S.; Kim, D.; Lee, S. B.; Han, S. W. *ACS Nano* **2012**, *6*, 2410−2419.
(6) Sekol, R. C.; Li, X.; Cohen, P.; Doubek, G.; Carmo, M.; Taylor, A. D. *Appl. Catal., B* **2013**, *138*−*139*, 285−293.
(7) Zhang, Z.; More, K. L.; Sun, K.; Wu, Z.; Li, W. *Chem. Mater.* **2011**, *23*, 1570−1577.
(8) Gu, S.; Cai, R.; Luo, T.; Chen, Z.; Sun, M.; Liu, Y.; He, G.; Yan, Y. *Angew. Chem., Int. Ed.* **2009**, *48*, 6499−6502.
(9) Varcoe, J. R.; Slade, R. C. T.; Lam How Yee, E. *Chem. Commun.* **2006**, 1428−1429.
(10) Varcoe, J. R.; Slade, R. C. T. *Electrochem. Commun.* **2006**, *8*, 839−843.
(11) Shim, J. H.; Kim, J.; Lee, C.; Lee, Y. *Chem. Mater.* **2011**, *23*, 4694−4700.
(12) Sun, W.; Hsu, A.; Chen, R. *J. Power Sources* **2011**, *196*, 4491−4498.
(13) Koenigsmann, C.; Santulli, A. C.; Sutter, E.; Wong, S. S. *ACS Nano* **2011**, *5*, 7471−7487.
(14) Halder, A.; Patra, S.; Viswanath, B.; Munichandraiah, N.; Ravishankar, N. *Nanoscale* **2011**, *3*, 725−730.
(15) Lee, K.; Kang, S. W.; Lee, S. U.; Park, K. H.; Lee, Y. W.; Han, S. W. *ACS Appl. Mater. Interfaces* **2012**, *4*, 4208−4214.
(16) Chen, L.; Guo, H.; Fujita, T.; Hirata, A.; Zhang, W.; Inoue, A.; Chen, M. *Adv. Funct. Mater.* **2011**, *21*, 4364−4370.
(17) Zhang, L.; Hou, F.; Tan, Y. *Chem. Commun.* **2012**, *48*, 7152−7154.
(18) Caixia, X.; Yan, Z.; Liqiang, X.; Xiufang, B.; Houyi, M.; Yi, D. *Chem. Mater.* **2009**, *21*, 3110−3116.
(19) Fouda-Onana, F.; Bah, S.; Savadogo, O. *J. Electroanal. Chem.* **2009**, *636*, 1−9.
(20) Shih, Z.-Y.; Wang, C.-W.; Xu, G.; Chang, H.-T. *J. Mater. Chem. A* **2013**, *1*, 4773−4778.
(21) Neergat, M.; Gunasekar, V.; Rahul, R. *J. Electroanal. Chem.* **2011**, *658*, 25−32.
(22) Shao, M.-H.; Sasaki, K.; Adzic, R. R. *J. Am. Chem. Soc.* **2006**, *128*, 3526−3527.
(23) Fernández, J. L.; Raghuveer, V.; Manthiram, A.; Bard, A. J. *J. Am. Chem. Soc.* **2005**, *127*, 13100−13101.
(24) Slanac, D. A.; Hardin, W. G.; Johnston, K. P.; Stevenson, K. J. *J. Am. Chem. Soc.* **2012**, *134*, 9812−9819.
(25) Kim, J.-H.; Bryan, W. W.; Chung, H.-W.; Park, C. Y.; Jacobson, A. J.; Lee, T. R. *ACS Appl. Mater. Interfaces* **2009**, *1*, 1063−1069.
(26) Koenigsmann, C.; Sutter, E.; Adzic, R. R.; Wong, S. S. *J. Phys. Chem. C* **2012**, *116*, 15297−15306.
(27) Liu, M.; Lu, Y.; Chen, W. *Adv. Funct. Mater.* **2013**, *23*, 1289−1296.
(28) Xu, C.; Wang, L.; Wang, R.; Wang, K.; Zhang, Y.; Tian, F.; Ding, Y. *Adv. Mater.* **2009**, *21*, 2165−2169.
(29) Sun, Y.; Xia, Y. *J. Am. Chem. Soc.* **2004**, *126*, 3892−3901.
(30) Mayers, B.; Jiang, X.; Sunderland, D.; Cattle, B.; Xia, Y. *J. Am. Chem. Soc.* **2003**, *125*, 13364−13365.
(31) Zhang, H.; Jin, M.; Liu, H.; Wang, J.; Kim, M. J.; Yang, D.; Xie, Z.; Liu, J.; Xia, Y. *ACS Nano* **2011**, *5*, 8212−8222.
(32) Zhang, W.; Yang, J.; Lu, X. *ACS Nano* **2012**, *6*, 7397−7405.
(33) Chen, G.; Xia, D.; Nie, Z.; Wang, Z.; Wang, L.; Zhang, L.; Zhang, J. *Chem. Mater.* **2007**, *19*, 1840−1844.
(34) Vasquez, Y.; Sra, A. K.; Schaak, R. E. *J. Am. Chem. Soc.* **2005**, *127*, 12504−12505.
(35) Li, H.; Lin, H.; Hu, Y.; Li, H.; Li, P.; Zhou, X. *J. Mater. Chem.* **2011**, *21*, 18447−18453.
(36) Yang, J.; Chen, X.; Yang, X.; Ying, J. Y. *Energy Environ. Sci.* **2012**, *5*, 8976−8981.
(37) Li, H.; Zhu, Z.; Liu, J.; Xie, S.; Li, H. *J. Mater. Chem.* **2010**, *20*, 4366−4370.
(38) Yang, L.; Hu, C.-G.; Wang, J.-L.; Yang, Z.-X.; Guo, Y.-M.; Bai, Z.-Y.; Wang, K. *Chem. Commun.* **2011**, *47*, 8581−8583.
(39) Paulus, U. A.; Schmidt, T. J.; Gasteiger, H. A.; Behm, R. J. *J. Electroanal. Chem.* **2001**, *495*, 134−145.
(40) Wang, M.; Zhang, W.; Wang, J.; Minett, A.; Lo, V.; Liu, H.; Chen, J. *J. Mater. Chem. A* **2013**, *1*, 2391−2394.
(41) Zhu, L. D.; Zhao, T. S.; Xu, J. B.; Liang, Z. X. *J. Power Sources* **2009**, *187*, 80−84.
(42) Liu, Y.; Hangarter, C. M.; Bertocci, U.; Moffat, T. P. *J. Phys. Chem. C* **2012**, *116*, 7848−7862.